

Light-propagation management in coupled waveguide arrays: Quantitative experimental and theoretical assessment from band structures to functional patterns

Jean-Marie Moison,¹ Nadia Belabas,¹ Juan Ariel Levenson,¹ and Christophe Minot^{1,2}

¹Laboratory for Photonics and Nanostructures, CNRS UPR20, Route de Nozay, F-91460 Marcoussis, France

²Institut Telecom/Telecom ParisTech, 46 rue Barrault, 75634 Paris Cedex 13, France

(Received 22 May 2012; published 10 September 2012)

We assess the band structure of arrays of coupled optical waveguides both by *ab initio* calculations and by experiments, with an excellent quantitative agreement without any adjustable physical parameter. The band structures we obtain can deviate strongly from the expectations of the standard coupled mode theory approximation, but we describe them efficiently by a few parameters within an extended coupled mode theory. We also demonstrate that this description is in turn a firm and simple basis for accurate beam management in functional patterns of coupled waveguides, in full accordance with their design.

DOI: [10.1103/PhysRevA.86.033811](https://doi.org/10.1103/PhysRevA.86.033811)

PACS number(s): 42.79.Gn, 42.82.Et, 42.25.Bs, 71.20.-b

I. INTRODUCTION

Arrays of weakly coupled optical waveguides are simple realizations of the ubiquitous paradigm of the lattice of coupled objects. Their ability to mimic complex systems—atomic or others—with a very small number of elements makes them remarkably fruitful model systems for demonstrating fundamental effects such as quasifree propagation of light, diffraction engineering [1–3], Bloch oscillations, quantum mechanical decay, Anderson localization, and Rabi oscillations [4–9], as well as routing optical signals [10–12]. In a further step, following the introduction of “defects” in arrays [13], we have proposed the systematic patterning of the coupling for engineering the propagation of guided light [14]. Inside this structured metamaterial, wave packets or “beams” can be redirected by interfaces [15,16], guided by channels [17], focused by lenslike patterns, steered by control beams, etc. This global framework, which we call “guidonics” in analogy to electronics or free-space optics, offers many beam management configurations and applications. However, they depend critically on the capacity to model the propagation of beams in a simple but accurate way.

Indeed a key to the success of weakly coupled waveguide arrays is the general claim that they can be treated by the standard coupled mode theory (CMT), whose main assumption is a weak coupling between first-neighbor waveguides only. This allows drastic approximations so propagation can be described by simple equations—the discrete Schrödinger equations—involving only a single parameter, the coupling coefficient C . However, most actual arrays, which aim at high couplings providing strong effects and short devices for high density and low losses, do not operate in the true weak-coupling regime [18]. Anyway CMT is unfit for describing advanced effects such as multiband effects, gap or Floquet-Bloch solitons, and multiband or multigap solitons or vortices [19]. Hence the full and accurate determination of array band structures is nonetheless required to go beyond mere qualitative assessments and to describe and demonstrate on a quantitative basis the various effects.

Waveguide arrays, being one-dimensional (1D) periodic systems, are best described by the Floquet-Bloch (FB) analysis. We consider 1D lattices of identical, straight, parallel, and

monomode waveguides, with the period S . X and Z axes are, respectively, normal and parallel to the waveguide axis. FB modes with a wave envelope $\exp(iK_x X + iK_z Z)$ propagate freely when K_x and K_z are related by the diffraction relation $K_z(K_x)$, also called the dispersion relation. This perturbation of the quasiparabolic relation of the nonstructured space described by a mere effective index involves allowed bands and forbidden gaps (see an example in Fig. 1), as in any 1D photonic band-gap system. This set of bands constitutes the band structure. In the CMT approximation for weak couplings, only the upper band is considered and it has a cosine shape.

Although FB modes cannot be implemented as such, they form a very efficient basis for the description of light propagation, with the band structure as a backbone. Indeed as we demonstrate in Sec. IV the shape of a band directly controls the propagation of beams within the array. The calculation and experimental validation of this structure—and especially the most relevant upper band—are therefore key issues. However, surprisingly enough, very little has been reported about its calculation and its experimental measurement (see an extended bibliography in the next section), and still less—a single article [20]—about the convergence of the two approaches, with disappointing results for the upper band.

We concentrate the present work on this experiment-model convergence, keeping in mind that, beyond the basic determination of the properties of homogeneous arrays, the analysis scheme—calculation combined with experimental probing method—must also remain efficient on advanced patterned arrays involving a combination of several band structures. Our results demonstrate that an excellent convergence can indeed be obtained on homogeneous arrays. Our demonstration relies (i) on the development of a specific two-dimensional effective-index model validated on the upper band by reference to results of *ab initio* calculations and (ii) on original fully quantitative measurements performed on well-characterized arrays.

In the following, we first review and analyze the principles, the advantages, and the drawbacks of the known schemes used to probe the band structure of waveguide arrays, and especially the “head-on” scheme that we favor as giving the best experimental signature of the upper bands (Sec. II). We next describe our own calculation of the band structure (Sec. III) and our prediction of experimental signatures using

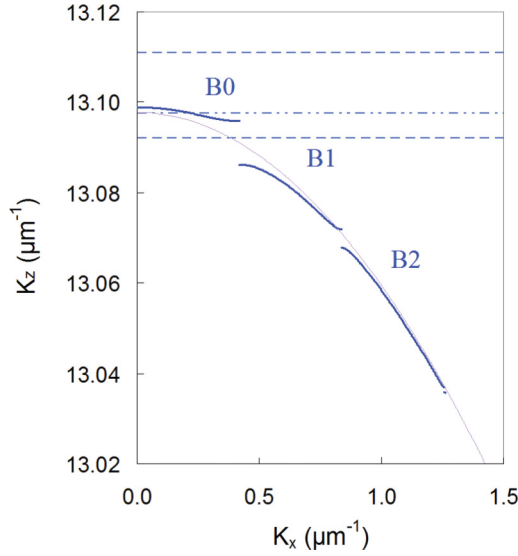


FIG. 1. (Color online) Typical band structure of a waveguide array (see details in caption of Fig. 3). The blue partial curves labeled B0, B1, and B2 are the bands. The continuous purple curve is the diffraction relation of the equivalent planar waveguide. Dashed horizontal lines indicate the levels of the planar waveguides and the dash-dot line is the level of the isolated ridge waveguide.

the calculated bands combined with a beam propagation framework (Sec. IV). After a description of our experimental setup and of our test waveguide arrays, we compare the data we obtain on homogeneous arrays with our expectations, in the two polarizations and over a wide range of coupling constants (Sec. V). The excellent quantitative agreement obtained is discussed in Sec. VI. It validates both calculation and experiment and clarifies the ways various bands are excited depending on initial conditions, thus giving a criterion to safe operation within the upper band. It also conclusively confirms the nonweak nature of the coupling in standard literature arrays. Therefore even the simplest propagation properties such as the propagation direction of a weakly divergent beam cannot be forecast within CMT alone but requires the straightforward extension (eCMT) we proposed in a previous work [18]. We finally report in Sec. VII preliminary results showing that this whole framework enables us to predict accurately the signatures of various guidonic functional patterns.

II. PROBING THE BAND STRUCTURE

Various schemes have been proposed to probe the arrays' band structure (Fig. 2). They all rely on the excitation of “beams” localized in a limited but rather large (waist $\gg S$) region of space, which can then be expressed as wave packets, i.e., as the combination of FB modes with a limited extension in $\{K_x, K_z\}$ around the initial $\{K_{x0}, K_{z0}\}$.

The first and by far most widely used coupling scheme is the “head-on coupling” [21] from air at the $Z = 0$ plane of a Gaussian free-space beam with a large waist W_0 and an initial wave vector K_{x0} set by its incidence angle θ ($K_{x0} = 2\pi \sin\theta/\lambda$). Setting K_{x0} corresponds to a vertical cross section of the band structure [Fig. 2(a)], which selects one wave vector $\{K_{x0}, K_z^{[m]}(K_{x0})\}$ per band m . As explained in

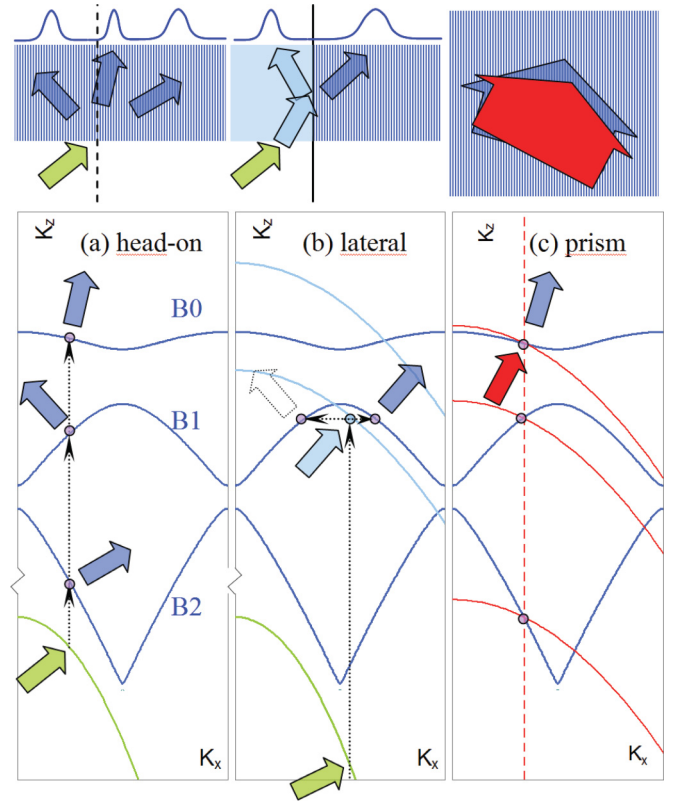


FIG. 2. (Color online) Schematics of selection rules for the three coupling schemes. The folded bands (dark blue lines) are those of an array described in Sec. III (Fig. 3). (a) Head-on coupling: Injection is made from air and sets K_{x0} ; three guidonic beams are generated at wave vectors noted by purple dots, with directions indicated by arrows. The green lower parabolic line is the diffraction relation of air, shown on a shifted scale. (b) Lateral coupling: Injection is made from air to the lower planar waveguide (light blue left-hand-side region, middle light blue parabolic diffraction relation) and coupling to the array selects K_{z0} . Only one guidonic beam is generated since a backward-going beam cannot exist. The light blue upper parabolic line is the diffraction relation of the upper planar waveguide. (c) Prism coupling: Light is coupled evanescently from the total reflection face of an adjacent prism. The angle ψ between the incidence plane and array sets a first quasivertical selection line (dotted quasivertical red line). Scanning the incidence angle φ on the prism scans the modulus of $\{K_{x0}, K_{z0}\}$ (red parabolic curves are isomodulus curves corresponding to three values of φ), and at resonance, both line and curve intersect with a band (purple dot).

detail in the next sections, one observes after propagation an output intensity profile $I(X)$, which is a combination of beam patterns whose position and width probe the first and second derivatives of the bands. Scanning θ and hence K_{x0} yields the $I(K_{x0}, X)$ map which we will address as the experimental guidonic signature (GS) of the waveguide array.

A second similar scheme suggested by Zengerle [22] and implemented by Mandelik *et al.* [23–25] is the “lateral coupling,” i.e., injection from air at the $Z = 0$ plane with an incidence angle θ into a waveguideless region of index n_{inj} at the $X = 0$ plane, and then to the array. When this beam encounters the array, it sets an initial wave vector $K_{z0} = 2\pi/\lambda n_{inj} \cos[a \sin(\sin\theta/n_{inj})]$. In this horizontal

cross-section scheme [Fig. 2(b)], only one single band m is excited, and even though several wave vectors $\{K_{x0}^{(m)}(K_{z0}), K_{z0}\}$ are obtained, only one forward beam is observed due to the periodicity of the band. Here again, the derivatives of this band can be extracted from the output profile map $I(K_{x0}, X)$. The two first schemes resemble conventional ray refraction measurement.

In the third well-known “prism coupling” scheme implemented on waveguide arrays by Rüter and co-workers [20], [26] the whole array is excited by optical tunneling of a very wide external beam through an air gap between a prism and the waveguide array [Fig. 2(c)]. Since the excitation is delocalized in the array plane, both K_{x0} and K_{z0} are set by the angle φ of incidence on the prism and the angle ψ of the array with the total reflection plane. In view of the small useful K_z range, ψ approximately sets K_{x0} and scanning φ scans the modulus of $\{K_{x0}, K_{z0}\}$ and hence K_{z0} . The guidonic beam generated is not monitored. Information is carried by the loss seen on the reflected beam or coupling efficiency, which rises when the wave vector $\{K_{x0}, K_{z0}\}$ lies in a band and therefore can actually propagate in the array. The signature is here an $I(K_{x0}, K_{z0})$ map. This scheme rather resembles absorption spectroscopy.

All three schemes have their advantages and drawbacks. The prism coupling scheme is obviously the most straightforward and efficient: The whole band structure can be reconstructed by merely pointing transmission maxima. Single-channel excitation has been obtained with this scheme [27], which permits selective excitation of a given zone in patterned arrays. On the other hand, this scheme requires a complex setup involving especially a prism with an index larger than the effective index of the upper band, which is not altogether obvious. For the widely used III-V semiconductor arrays, this would require, for instance, a large silicon prism. From published data, resolution and accuracy for the upper band also do not seem to be high enough. In addition, close contact of the prism with the array may be a noticeable perturbation to FB wave propagation.

The lateral coupling scheme also scans the whole band structure, though the key upper band is out of reach when light is not injected from a higher-index region but more simply from the continuum [23–25]. It yields only derivatives of the band structure, which is not altogether inconvenient since they describe what is really important experimentwise, the direction and divergence of beams. Accuracy and resolution seem correct, but no quantitative analysis has ever been reported. The analysis of patterned arrays—or at least of the simple ones where C is varied only in the X direction—would not be easy since that lateral injection can only be made in the leftmost or rightmost pattern and not directly in inner patterns.

Finally, if the head-on coupling scheme seems *a priori* less efficient—it does not reveal band gaps, and combines information from all bands—it naturally probes the upper band and it is also by far the easiest to implement and the most promising for application to advanced guidonic patterns. Therefore this scheme remains the most widely used and several articles we have reviewed now have reported early implicit experimental signatures.

In a pioneering work [3] Eisenberg *et al.* used various AlGaAs waveguide arrays tilted with respect to the normal

to the interface in order to vary K_{x0} , a substitute method for changing the incidence angle. Only a few points of the Brillouin zone separated by $K_{x0}S = \pi/2$ were probed. A comparison of experimental output profiles with CMT expectations showed a fair qualitative agreement, except at high K_{x0} where second-band excitation was suspected. Pertsch *et al.* [21] presented the first complete GS of polymer waveguide arrays in the $K_{x0}S [-3/2\pi, 3/2\pi]$ range. The result was rather compatible with CMT, which allowed to extract a coupling coefficient. No indication of second-band excitation was noted. Beam deviation-divergence formulas were cited, but no attempt at fitting the data was made. Mandelik *et al.* [23] reported the first GS in the $[0, 2\pi]$ range showing explicitly and quite clearly the second-band excitation at high $K_{x0}S$ on AlGaAs waveguide arrays. Though calculated band structures were shown, no comparison between calculation and experiment was made. On similar AlGaAs waveguide arrays Sukhorukov *et al.* [28] reported a qualitative description of GS features (position, width, coupling efficiency) and a GS. Meier *et al.* [29] reported a GS in the $[-\pi, \pi]$ range showing a clear deviation from CMT, as seen from the strongly nonsine shape of the trace, without interpretation or calculation. A similar observation was reported by Suntsov [30]. Iwanow *et al.* [31] reported another GS in the $[-\pi, \pi]$ range on periodically-poled lithium niobate; agreement with CMT was correct both on the deviation and on the divergence variations, but using a mere adjustable coupling coefficient. Two other articles have reported GSs involving soliton formation [32] or interface modes [30]. In conclusion, as we already stated, to our knowledge there is at present almost no theoretical assessment of the GSs and no successful quantitative comparison between calculated and experimental GSs. This is nevertheless a prerequisite for the design and validation of functional patterns. In the next sections, we show how the models we devised to predict the GSs and their experimental confirmation close this gap.

III. CALCULATION OF THE BAND STRUCTURE

Several calculations have been developed to predict guidonic band structures, though most of them—e.g., the extension of Yeh’s method [33] in a transverse dimension [23], [34], solution of paraxial wave equations [35]—have not been compared with experimental data. To our knowledge the only one which has indeed been tested is the resolution of wave equations with a finite difference method [20], which gives a good prediction of the second and third band, but oddly enough a poor one of the upper band.

We implemented a full calculation of the band structure in three steps. We first used band sampling [18] by determining the modes of a few-waveguide system [36] through finite-element method (FEM) solution of Maxwell’s equations. This method is quite straightforward and robust, but it provides mostly only the confined bands since the other bands are hidden among unwanted modes. With this reference, we validated [18] another method, also limited to the upper band, that allows us to calculate arrays of strip-loaded (“shallow-ridge”) waveguides or buried-bars waveguides. This extension of CMT (eCMT) includes the influence of second neighbors and mode overlaps. It uses only the isolated waveguide mode as a basis for analytical calculations of the

complete upper band. Within CMT, the upper band has a cosine shape $K_z = \beta_{iw} + 2C \cos(K_x S)$ where β_{iw} is the propagation constant of the isolated waveguide and the GS appears as a sine-shaped trace. The eCMT band shape involves additional dimensionless η , ξ , and ζ parameters that describe, respectively, the nearest-neighbor overlap, the self-coupling, and the next-nearest-neighbor coupling:

$$K_z = \beta_{irw} + C \frac{2 \cos(K_x S) + \xi + 2\zeta \cos(2K_x S)}{1 + 2\eta \cos(K_x S)}. \quad (1)$$

Those two calculations, FEM and eCMT, have in turn been validated on a wide range of experimental data based on diffraction of a narrow beam in the upper band. The latter can be explained by FB wave propagation over the whole band. They are nicely accounted for using an effective CMT with an apparent coupling coefficient C_{app} [37] which reflects the overall width of the band, not its actual shape. It is one aim of the present paper to give better insight into the band structure, the shape of the bands, and the beam propagation effects which demand to go beyond CMT and effective CMT.

Although very efficient, neither FEM nor eCMT provides us with the lower bands. For this purpose we have developed an original code for shallow-ridge waveguides that we call the two-dimensional effective-index (2DEI) model. This model is based on Yeh's theory [33] extended in a transverse dimension, and is inspired by electronic structure studies for superlattice miniband calculations in semiconductors with nonparabolic dispersion relations. In a first step, we use a transfer matrix method along Y to calculate effective indices for two different planar waveguides corresponding either to the initial unetched layer stack (the limit case of infinitely wide ridges) or to the fully etched stack (the limit case of zero-width ridges) which give the upper and lower confinement effective index, respectively. Then we apply again Yeh's approach along X to an infinite lattice with alternating effective-index values according to the desired ridge width and separation distance. Along both X and Y , the matching conditions at the interfaces depend on the polarization, either transverse electric (TE) or transverse magnetic (TM). In the X direction, they are only satisfied on the average over the interface areas.

A good description of the upper bands can be expected for strongly monomode planar structures and shallow ridges which exhibit weak polarization mixing, provided the higher-order planar modes, e.g., those confined in the substrate, remain far enough from the coupling region and can be neglected because they are strongly evanescent at the interfaces. This condition can be true even in the continuum below the lower confinement effective index of the planar structures. When applied to our structures, possible limitations of the accuracy of our code arise from two main factors. 2DEI considers only the localized states as a basis and not the delocalized ones which are all the more important as one considers lower bands. 2DEI also separates arbitrarily TE and TM polarizations, with the same shortcomings. In practice, small discrepancies with the FEM method arise regarding band shifts and overlap integrals at short distances (see Sec. VI). Actually, projection onto a single planar mode in the etched and unetched regions is an approximation which cannot provide truly exact profiles for the FB modes in the vicinity of the interfaces between the two regions. A much larger basis would be required to

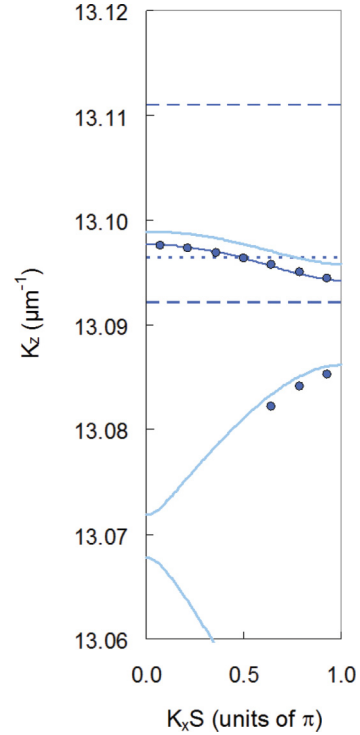


FIG. 3. (Color online) Folded band structure of an InP/InGaAsP waveguide array with $S = 7.5 \mu\text{m}$ (see Sec. V) for $\lambda = 1.55 \mu\text{m}$ and TE polarization. The three light blue (light gray) curves are obtained from the 2DEI model, the blue dots from *ab initio* FEM calculations, and the dark blue (dark gray) curve from the extended-CMT model. Lines indicate the levels of the planar waveguides (dashed lines) and of the isolated ridge waveguide (dotted line).

satisfy the matching conditions and this would give rise to renormalization effects (band shifts) and changes of short distance correlations (overlap integrals at small interguide spacings).

Figure 3 shows a typical example obtained on a waveguide we use in the experiments. Compared to the reference given by the combination of FEM and eCMT calculations, the position and shape of the upper band and of part of the second band are correctly predicted, to a small vertical shift. This shift is nevertheless unimportant since actual beam effects depend only on the derivatives of the bands as we will see in Sec. IV.

The agreement between FEM and 2DEI calculations can be assessed on a more quantitative basis in the framework of eCMT by comparing the eCMT parameters (C , η , ξ , and ζ) calculated by either method from the respective upper bands. The values obtained for the test arrays used here in the TE polarization are shown in Table I. Taking FEM data as a reference, 2DEI overestimates the nonorthogonality coefficient η in the most coupled arrays, as expected from the above discussion. However, the overall agreement on the eCMT parameters is quite satisfactory. In particular, the apparent coupling coefficient C_{app} can be correctly deduced from the vertical extension of the band.

Finally our 2DEI model provides us through a simple and fast calculation with the best possible FB modes in the chosen projection basis and, as experiments will also demonstrate, with correct values of (i) the shapes of the various bands

TABLE I. eCMT band parameters extracted from fits of the FEM and 2DEI band in TE polarization. $\Delta\beta/4$ is 1/4 of the band vertical extension and C_{app} from experiments (Ref. [37]).

S μm	C mm^{-1}	η	ξ	ζ	$\Delta\beta/4$ mm^{-1}	C_{app} mm^{-1}
5 FEM	1.77	0.32	0.13	0.24	2.42	2.70
5 2DEI	1.77	0.45	0.09	0.19	2.57	
7.5 FEM	0.76	0.20	0.05	0.09	0.85	0.86
7.5 2DEI	0.67	0.23	0.03	0.07	0.77	
9 FEM	0.45	0.14	0.03	0.05	0.48	0.48
9 2DEI	0.38	0.15	0.02	0.04	0.41	

$K_z^{[J]}(K_x)$, not only the upper one, and (ii) the overlap of the corresponding modes with a broad enough Gaussian input, and hence the optical input coupling efficiencies. We now show that based on this information, the envelope of the GS can be fully determined without any additional parameter.

IV. FROM THE BAND STRUCTURE TO THE GUIDONIC SIGNATURE

Guidonic signatures have not yet been fully modeled as such. However, ingredients necessary for predicting them knowing the band structure can be found in the literature (see, for instance, [3,21,28,38]). In this section, we assemble these ingredients and additional ones in a rigorous fashion based on the description by FB waves and show that guidonic signatures can be derived analytically from the results of the band structure calculation. Our complete derivation relies on a very general projection principle and it is therefore valid for any kind of waveguide array.

Following launching at $Z = 0$ with an initial wave vector K_{x0} in a Gaussian amplitude envelope of waist W_0 , several beams are generated, each one corresponding to a single band J . Those beams are the combination of FB modes with a limited extension in K_x around the initial wave vector K_{x0} and hence around $K_z(J, K_{x0})$ selected by the selection rules of Fig. 2(a). We consider reasonable conditions of well-collimated beams ($2\pi W_0 \gg S$), negligible overlap between different band modes—a significant overlap occurs only near the Brillouin zone critical points—and weak wave vector dependence of the periodic parts U of the FB modes. Under these conditions, we show in Appendix A that the output intensity for band J can be written as:

$$I(J, K_{x0}, X, Y, Z) \approx |U(X, Y)|^2 T(J, K_{x0}) \times \frac{S^2}{\pi W_0 W(Z)} e^{-2| \frac{X+D_1 Z}{W(Z)} |^2}, \quad (2)$$

where T is the optical input coupling efficiency, D_1 and D_2 are the first and second derivatives of band J at K_{x0} , and the waist evolution is

$$W(J, K_{x0}, Z) = W_0 \sqrt{1 + \left(\frac{2D_2 Z}{W_0^2} \right)^2}. \quad (3)$$

This intensity distribution first reflects the transversal intensity pattern $|U(X, Y)|^2$ of the underlying (J, K_{x0}) FB mode, which can be distinctly observed experimentally when the individual waveguides are well separated (see the data

for $S = 9 \mu\text{m}$ and $S = 7.5 \mu\text{m}$ in Fig. 6). Since we wish to describe rather wide beams spreading over several waveguides, in the following we omit this term and consider only the other ones, i.e., we use an envelope description. Propagation of wide beams can then be treated within general wave theory by a calculation analog to its counterpart in free-space optics. As seen from Eq. (2) each beam corresponding to a single band propagates along a straight line with a Gaussian divergence. Its specific properties are as follows: mean wave vector $\{K_{x0}, K_z(J, K_{x0})\}$, mean direction given by $X/Z = -D_1(J, K_{x0})$, divergence given by Eq. (3), and coupling efficiency $T(J, K_{x0})$ given by the overlap of the mode with the input field. Though formally similar to conventional Gaussian beams, guidonic beams have nontrivial behaviors. Due to the shape of the bands, the beam deviation has an upper limit, and the divergence depends on K_{x0} ; it even vanishes at inflection points of the bands (diffractionless propagation [3]).

After propagation up to the sample length $Z = L$, the envelope of the output profile appears as a combination of Gaussian patterns corresponding to the various excited bands [see top of Fig. 2(a)] which can be reconstructed by the above formulas. The model GS is taken as the $I(K_{x0}S, X/L)$ map. It thus deals with dimensionless data and readily displays the first derivative D_1 of the bands and the tangent of the deviation angle. The model GS involves various traces weighted by the coupling efficiencies. Around $K_{x0}S = 0$ (unstaggered mode), only the upper band is excited. Around $K_{x0}S = \pi$, its contribution begins to vanish to be replaced by the second band contribution [38], in turn replaced by the third one around $K_{x0}S = 2\pi$ (Fig. 4, top).

It may be stressed that for most of our arrays and for most of the literature structures we could analyze, the upper-band trace differs significantly from what is expected in the genuine weak-coupling approximation (Fig. 4, bottom). The GS trace is then a distorted sine with a vertical span scaled by $4CS$ ($4C_{\text{app}}S$, in fact). Since in most literature data $0.01 < CS < 0.001$ ($CS \ll 1$ is indeed a prerequisite for the CMT) the spans and actual beam deviation angles are small ($< 1.5^\circ$). For large beams, the vertical width of the trace (i.e., the width of the output beam) is constant while for medium-sized beams, it oscillates between maxima for $K_{x0}S = p\pi$ and minima ($= W_0/Z$, i.e., no divergence) for $K_{x0}S = \pi/2 + p\pi$, following the variations of D_2 which is scaled by $2CS^2$. These considerations also help scaling the experimental conditions. Obtaining clearly the first derivative from the deviation obviously requires the deviation to be larger than the width due to the minimum waist $2CS > W_0/L$, i.e., $W_0/S < 2CL$ or $W_0/S < L/L_c$, where L_c is the average coupling length; in view of literature data this means $W_0/S < 10$. On the other hand, too narrow a beam induces too large a divergence at $K_{x0}S = p\pi$, which again blurs the information; hence a condition $W_0/S > 1.5$. The optimum visibility is thus obtained at medium waists.

V. EXPERIMENTAL SETUP AND RESULTS

Our test strip-loaded waveguide arrays involve an InP/InGaAsP “shallow-ridge” design. All details on their structure and on their properties are given in Refs. [18,37]. They are typical of the most widely used waveguides,

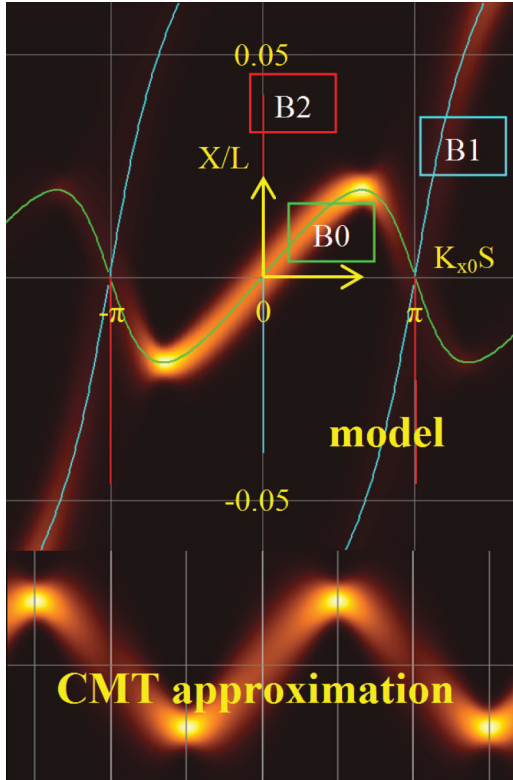


FIG. 4. (Color online) (Top) Typical envelope GS calculated using the 2DEI band structure of Fig. 3 combined with the beam framework at $W_0/S \sim 2$. The contributions of the three upper bands are shown. Their center is marked by lines labeled B0, B1, and B2. (Bottom) CMT approximation obtained by taking for the shape of the upper band a mere cosine curve with the same amplitude as the real band.

i.e., semiconductor-based ones. Array periods are 5, 7.5, or $9 \mu\text{m}$. The experimental setup is sketched in Fig. 5.

Light from a $1.55\text{-}\mu\text{m}$ laser diode is input in the array via a polarization controller (polarizer plus $\lambda/2$ and $\lambda/4$ wave plates) tuned for instance to the horizontal ($//X$, TE) polarization and the cleaved end of a microstructured fiber, designed to have a single mode of large waist $W_0 = 15 \mu\text{m}$ (ThorLabs). This fiber is mounted on a rotation stage, the center of which lies in the input face of the array. The fiber end is located $80 \mu\text{m}$ away from this face, i.e., well inside the Rayleigh range (1.5 mm). We then expect a correct excitation by a tilted plane wave with a W_0 waist. W_0/S lies between 1.5 and 2.8, i.e., within the correct range of medium input waists deduced in Sec. IV.

Due to its circular input shape, light is also coupled to the substrate and a small part of it reaches the output end.

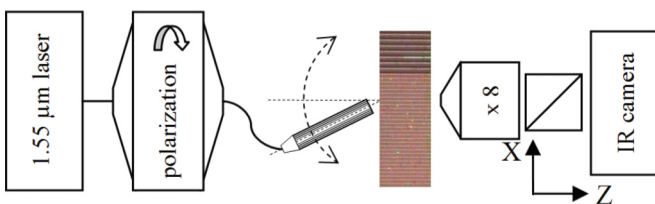


FIG. 5. (Color online) Sketch of the optical experimental setup.

Propagation length is $L \sim 3 \text{ mm}$. Considering the apparent coupling coefficients C_{app} , the reduced propagation lengths $L \cdot (C_{\text{app}})$ vary between 1.5 and 8.5, i.e., approximately three to 16 coupling lengths. Considering the divergence, we note that the maximum value of D_2 approximated by $2C_{\text{app}}S^2$ lies between one and three times W_0^2/L . Divergence should therefore remain limited.

The output face of the array is imaged onto an ir camera through a $8\times$ microscope objective and a polarizing cube tuned to either TE or TM polarization detection. Its center profile is stored after background subtraction. We can superimpose unambiguously the transmitted output pattern on the array pattern by directly shining $1.55\text{-}\mu\text{m}$ light on the output face. An analyzer cube suppresses any contribution of the unwanted polarization on output. This setup also allows us to visualize the input pattern. It is quite well approximated by a Gaussian mode of waist $W_0 = 14 \mu\text{m}$, in fair agreement with the expected value.

GSs are obtained by recording the output profile—i.e., a section of the output image along the center line of the modes of the waveguides—during $\pm 10^\circ$ scans of the input angle. Figure 6 shows typical results together with the corresponding simulations.

Except for a faint oblique trace of waveguiding in the substrate, most of the light at the output is concentrated in the waveguide region. Polarization studies confirm the polarization dependence of the coupling, and the very weak mixing: Upon injection by a given polarization, no contribution of the other one is detected on output, to within an accuracy of a few percent.

VI. DISCUSSION

The quantitative agreement between experiment and calculation is excellent for either polarization, while it must be stressed here again that calculations involve no adjustable parameter. The shape of the simulated GSs do superimpose on the experimental ones which confirms that our calculation gives an excellent prediction of the upper band—which was expected—and also of the second band. The agreement on divergence features is qualitatively correct: The low divergence at inflection points of the bands—maxima of the GS trace—shows as a marked intensity increase as expected. The excellent agreement between model and experiment also fully validates the technological process, which we previously checked using only C_{app} [37], i.e., the X/L span of the GS trace.

The succession of GSs also exemplifies clearly the progressive distortion of the upper band with increasing coupling, and hence the drift away from the genuine weak-coupling GS pattern (sine-shaped trace) to a medium-coupling pattern (distorted sine-shaped trace), and ultimately towards a fully coupled bulklike pattern (quasilinear trace). This is an explicit well-documented experimental demonstration of this effect. We can assess this effect on a quantitative basis in a simple analytical way using eCMT. The eCMT parameters of Table I demonstrate clearly the magnitude of the effect of second-order couplings: η is always important, and the other correction parameters, ζ and ξ , are rapidly no longer negligible.

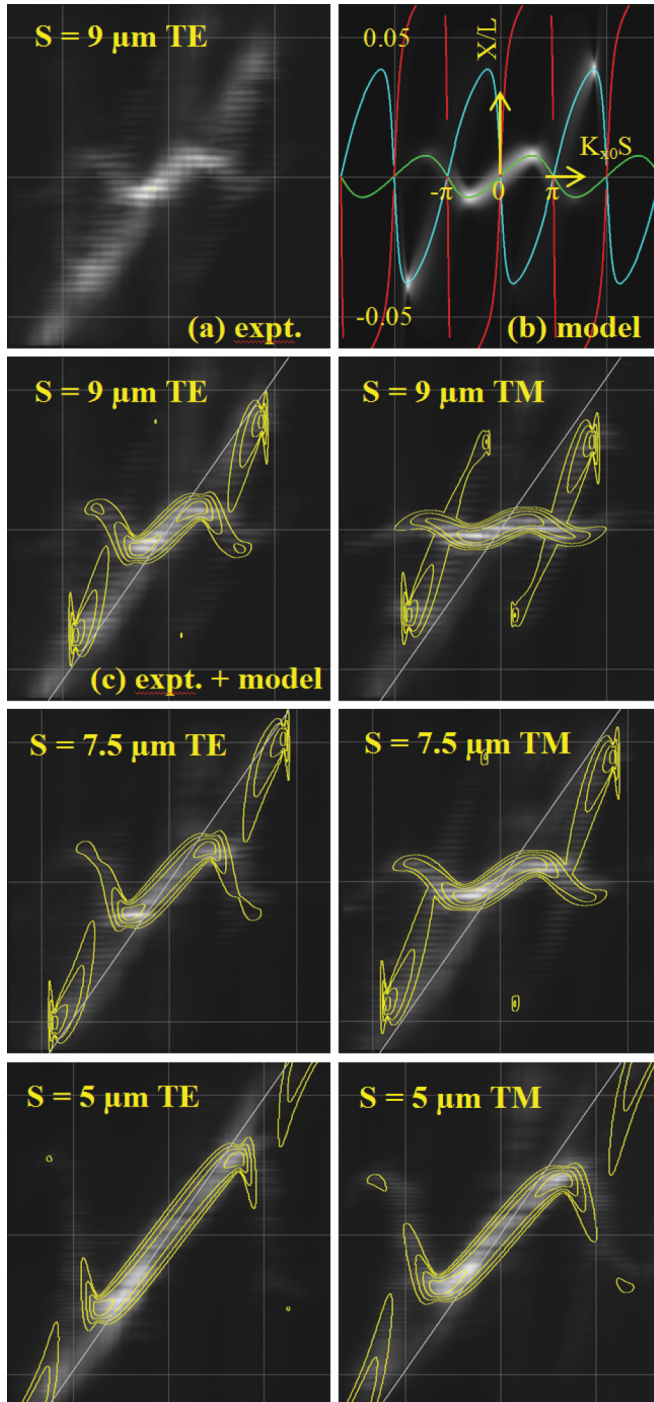


FIG. 6. (Color online) Guidonic signature of the test arrays for $S = 9 \mu\text{m}$ in TE polarization (input and output); ridge width is $2.0 \mu\text{m}$. Propagation length is 3.15 mm. (a) Experimental data. (b) Model GS obtained by 2DEI calculation plus beam envelope framework (see Secs. III and IV). Curves indicate the center of the traces, or derivative of the bands. (c) Superposition of experimental data with isointensity contours of the model for intensities at -2.5 , -5.0 , -7.5 , and -10 dB from the maximum; the oblique gray line is the signature of waveguiding in the substrate. Other panels same as (c) for other periods and polarizations.

Another important point is confirmed by the experiment. Using the appropriate medium input waists (Sec. IV), after

reduced propagation lengths $L \cdot (C_{\text{app}})$ which vary between 1.5 and 8.5, i.e., approximately three to 16 coupling lengths, we do obtain well-defined beams with the expected deviation. This is demonstrated by the limited vertical width of the traces in the GSs. Furthermore, in the range of the $K_{x0}S$ scan, only the upper band and the next one are efficiently excited, and the transition from upper-band excitation to lower-band excitation around $K_{x0}S = \pi$ is quite clear. Hence all possible beam directions in the upper band—the branch between the first negative minimum and the first positive maximum of the GS—can be generated by head-on coupling in a pure way, i.e., without exciting any other band. Therefore we can indeed accurately steer beams across waveguide arrays as required for light flow management and guidonic functions, thanks to our determination of the band structure. More precisely, the band shapes and the relative positions of the band edges make it possible to anticipate, respectively, the beam directions and the incidence angles where total internal reflection effects begin to occur. Based both on the knowledge of the band structure and on the beam management, we can now address the application of the head-on GS to patterned arrays and report preliminary results showing they can also be well predicted within our framework.

VII. PERSPECTIVES: THE SIGNATURE OF PATTERNED ARRAYS

Patterned arrays can be separated into two classes. In the first one, zones are large enough for beams to propagate according to the band structure of the corresponding infinite array. The simplest one is the junction between infinite zones (Fig. 7). Their envelope GS can then be predicted by our model with successions of interface crossings obeying space and phase conservation rules [14] and beam propagations; both can be calculated analytically knowing the band structures. Figure 7(b) shows that prediction is quite correct. After downward incidence ($K_{x0} < 0$), starting from $K_{x0}S = 0$ (normal incidence of the white arrow in inset) and increasing K_{x0} , we successively observe (i) pure transmission, as long as the beam reaches the output facet before the interface; then (ii) total reflection up to the critical angle, following the same dispersion relation but in the reverse direction; (iii) predominant refraction, the transmitted beam following the dispersion relation of the upper array; and (iv) return to pure reflection. Besides providing a good prediction of the experiment, the model clearly helps us understand these successive effects. As we see in the following, a still better fit can be obtained by solving numerically eCMT propagation equations, at the expense of this important physical insight.

The other class of patterns involves narrow zones—at least one—in which beam models are no longer useful. The most simple example of such patterns is the channel, equivalent of the optical waveguide, formed by a zone of high C surrounded by zones of low C (see Fig. 8).

We have shown [14] that mode analysis can be of some help here by pointing out critical points, but GSs can no longer be fully predicted. We have to rely on numerical simulations using eCMT coupled propagation equations, neglecting

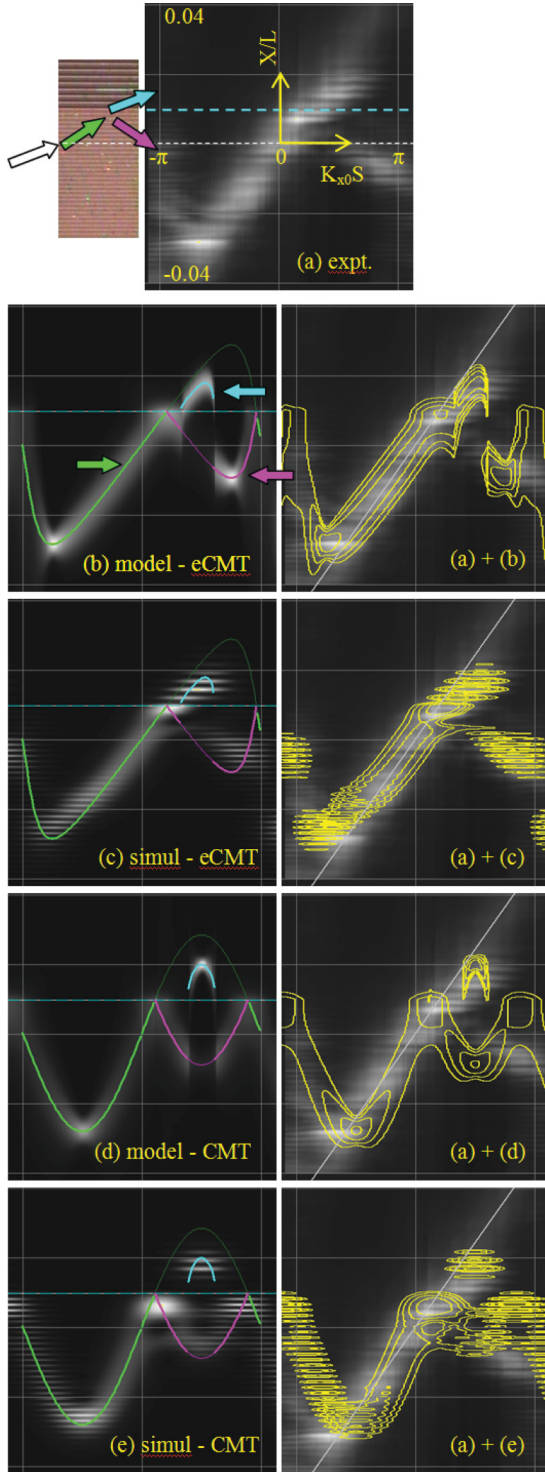


FIG. 7. (Color online) (a) GS of the interface between a $S = 5 \mu\text{m}$ zone (bottom) and a $S = 7.5 \mu\text{m}$ region (top) in TE polarization; ridge width is $1.5 \mu\text{m}$. Injection (dotted white line) is made $30 \mu\text{m}$ below the interface (dashed blue line). (b) Model envelope deduced from 2DEI data, taking into account only the upper band; regions corresponding to transmitted, refracted, and reflected beams are marked by green (light gray), blue (white), and purple (dark gray) arrows and lines. (c) Results of numerical simulation using eCMT. (d) and (e) same as (b) and (c), but using CMT. Right: Superposition of experimental data with isointensity contours of the simulation for intensities at -2.5 , -5.0 , -7.5 , and -10 dB from the maximum.

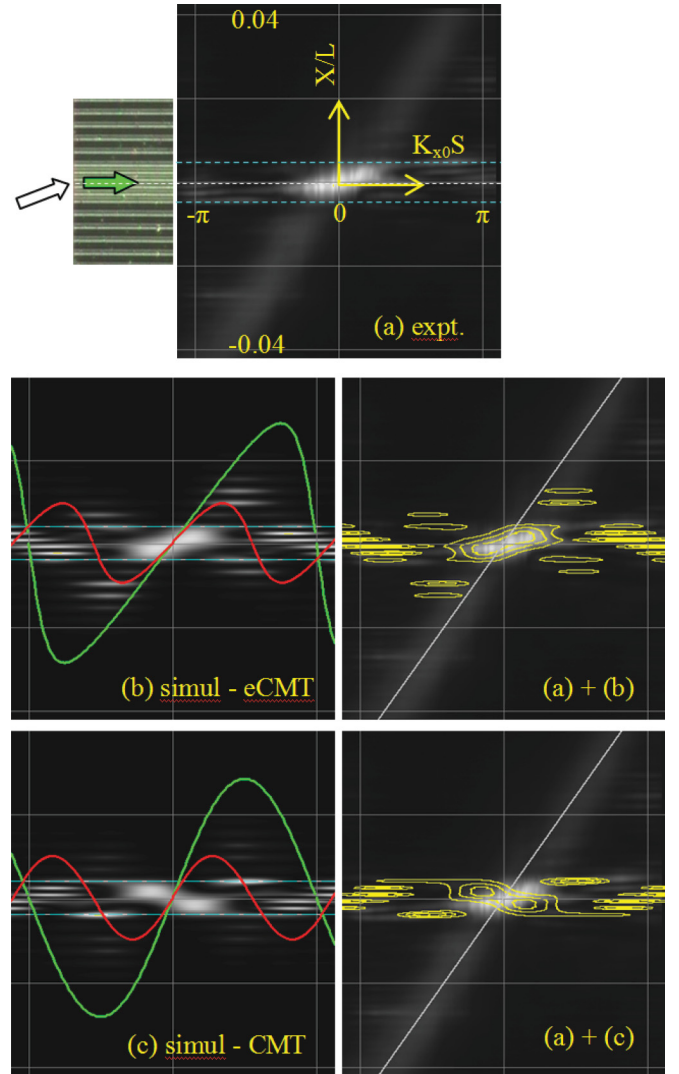


FIG. 8. (Color online) (a) GS of the channel formed by a $S = 5 \mu\text{m}$ zone between $S = 9 \mu\text{m}$ zones (top) in TE polarization; ridge width is $1.5 \mu\text{m}$. The channel is marked by the blue horizontal lines. Injection is made at its center. (b) Results of numerical simulation using eCMT. The red (dark gray) line is the trace of the low- C array; the green (light gray) line is the trace of the high- C array. (c) same as (b), but using CMT. Right: Superposition of experimental data with isointensity contours of the simulation for intensities at 0.8 , 0.6 , 0.4 , and 0.2 of the maximum.

contradirectional propagation. Those equations express the variation of \underline{a} , the vector of the modal amplitudes of the individual waveguides, according to

$$\underline{O} \frac{\partial}{\partial Z} \underline{a} = i \underline{C} \cdot \underline{a}, \quad (4)$$

where \underline{O} and \underline{C} are the overlap and coupling matrices. Within CMT, \underline{O} is the identity matrix and \underline{C} is tridiagonal with only C coefficients on the two diagonals. Within eCMT, \underline{O} is tridiagonal with ones on the main diagonal and ηC coefficients on adjacent diagonals, and \underline{C} is pentadiagonal with ξC coefficients on the main diagonal and \bar{C} and ζC coefficients on the four adjacent diagonals. The coefficients for each pattern are those of the corresponding infinite pattern determined

as described in Ref. [18], with special combinations at the interfaces (see Appendix B). Figures 8(b) and 8(c) show that prediction by eCMT using only the upper band renders quite well most features of the experiment, while mere CMT fails heavily. Note that this is also the case for the interface pattern [Figs. 7(c) and 7(d)], eCMT yielding significantly better overall agreement than the beam propagation approach because evanescent contributions at the interfaces are taken into account. Rather distinct mechanisms for total internal reflection in CMT and eCMT together with the different beam steering effects in either framework explain the dissimilar GSs and will be discussed elsewhere in more detail.

Finally, these data and calculations confirm that our patterned arrays do implement the designed functions of beam steering and beam guiding.

VIII. CONCLUSION

In this paper, we assess the band structure of coupled waveguide arrays on a quantitative basis. We report the calculation of this structure for shallow-ridge waveguide arrays, using the specially designed 2DEI method. Its combination with a collimated beam propagation technique allows us to predict the experimental signature of homogeneous arrays, i.e., the output deviation profile vs input wave vector map. Such a map provides a global view of propagation in the bands over the whole reciprocal space, in contrast to the usual transmission measurements after full diffraction of a narrow beam. The excellent quantitative agreement with actual experiments validates both calculation and experiment and clarifies the ways various bands are excited depending on initial conditions, thus giving a criterion to safe operation within the upper band while overlooking the other ones. It also definitely confirms the nonweak nature of the coupling in standard literature arrays, as anticipated theoretically. This means that even the simplest propagation properties such as the propagation direction of a weakly divergent beam, although keeping full significance, cannot be forecast within CMT alone. The high couplings required for getting strong effects and short devices could therefore have proven unusable due to excessive design complexity. However, the straightforward extension (eCMT) of CMT we propose accounts for actual propagation behaviors while remaining straightforward enough to design beam management guidonic devices by simple numerical means. Indeed, we show preliminary results which confirm that our approach remains operative on low-complexity patterned arrays, and that elementary guidonic functions such as steering and guiding can be implemented.

ACKNOWLEDGMENTS

The authors gratefully acknowledge the expertise and help of I. Sagnes, S. Bouchoule, E. Cambril, and J. C. Esnault in designing and processing the test waveguide arrays.

APPENDIX A

We sketch here the calculation of output intensity following excitation of a waveguide array by a Gaussian beam of light. The derivation justifies our envelope calculation for

propagation within the arrays and we spell out the necessary hypotheses. With the corresponding reasonable approximations, we thus establish that light flow can be treated along propagation in a homogeneous array as in a continuous medium and as a set of beams whose existence, direction, and divergence are deduced from the band structure.

The incident excitation field with initial wave vector K_{x0} can be decomposed into a sum of Bloch modes of the bands $\{J\}$ of the array

$$a_{K_{x0}}(X, Y, Z = 0) = \sum_{J, K_x} R_{J, K_x} e^{iK_x X} U(J, K_x, X, Y), \quad (\text{A1})$$

and propagates according to the diffraction relation of the band structure:

$$a_{K_{x0}}(X, Y, Z) = \sum_{J, K_x} R_{J, K_x} e^{iK_x X} U(J, K_x, X, Y) e^{iK_z(J, K_x)Z}. \quad (\text{A2})$$

For a Gaussian profile excitation field

$$a_{K_{x0}}(X, Y, Z = 0) = \sqrt{\frac{2}{\pi W_x W_y}} e^{-(X^2/W_x^2)} e^{-(Y^2/W_y^2)} e^{iK_{x0}X}, \quad (\text{A3})$$

$$\begin{aligned} R_{J, K_x} &= \sqrt{\frac{2}{\pi W_x W_y}} \iint U^*(J, K_x, X, Y) e^{-iK_x X} e^{-(X^2/W_x^2)} \\ &\quad \times e^{-(Y^2/W_y^2)} e^{iK_{x0}X} dX dY \\ &= \sum_p \overline{U_p^*}(J, K_x) e^{-\frac{W_x^2(K_x - K_{x0} + pG)^2}{4}}, \end{aligned} \quad (\text{A4})$$

where the bar denotes averaging in the Y direction, G is the basis vector of the reciprocal lattice in the X direction, and $U_p(J, K_x, X, Y)$ are the Fourier coefficients of $U(J, K_x, X, Y)$. K_x is in the first Brillouin zone and K_{x0} can take any value. The projection of the incident field on mode (J, K_x) thus has replicas around the successive orders of the reciprocal lattice $K_{x0} = K_x + pG$ with amplitudes $\overline{U_p^*}(J, K_x)$.

Propagation of the modes in the Z direction according to Eq. (A2) gives the output amplitude

$$\begin{aligned} a_{K_{x0}}(X, Y, Z) &= \frac{S}{2\pi} \sum_J \int_{-(\pi/S)}^{\pi/S} dK_x \sum_p F_p(J, K_x, X, Y) \\ &\quad \times e^{-\frac{W_x^2(K_x - K_{x0} + pG)^2}{4}} e^{iK_x X + iK_z(J, K_x)Z}, \end{aligned} \quad (\text{A5})$$

where $F_p(J, K_x, X, Y) = U(J, K_x, X, Y) \overline{U_p^*}(J, K_x)$.

Assuming a large waist W_x ($2\pi W_x \gg S$), integration is extended to infinity and the amplitudes nearby each order p ,

i.e., the Fourier transforms

$$a_{K_{x0},p}(X,Y,Z) \approx \frac{S}{2\pi} \sum_J \int dK_x F_p(J, K_x, X, Y) \times e^{-\frac{W_x^2(K_x - K_{x0} + pK_x)^2}{4} + iK_x X + iK_z(J, K_x)Z}, \quad (\text{A6})$$

are calculated independently. Indeed, for a given band J , interferences can only occur in vanishing Gaussian tails and only a single p contributes significantly to the sum over p of Eq. (A5).

$$a_{K_{x0}}(X,Y,Z) \approx \frac{S}{\pi} \sum_J \left\{ F_p[J, K_{x0}^{(D_1, D_2)}(Z, X), X, Y] + 2i \frac{\Delta X^{(J, K_{x0})}}{[W^{(J, K_{x0})}(Z)]^2} \frac{\partial F_p}{\partial K_x}[J, K_{x0}^{(D_1, D_2)}(Z, X), X, Y] \right\} \times \sqrt{\frac{\pi}{W_x^2 - 2iD_2^{(J, K_{x0})}Z}} e^{-\{(\Delta X^{(J, K_{x0})})^2/[W^{(J, K_{x0})}(Z)]^2\}} e^{i[K_{x0}X + (K_z^{(J, K_{x0})} - K_{x0})Z + K_{x0}^{(D_1, D_2)}(Z, X)\Delta X^{(J, K_{x0})}]}, \quad (\text{A8})$$

where

$$K_{x0}^{(D_1, D_2)}(Z, X) = K_{x0} - 2 \frac{\Delta X^{(J, K_{x0})} 2D_2^{(J, K_{x0})} Z}{W_x^2 [W^{(J, K_{x0})}(Z)]^2} \quad (\text{A9})$$

is a position dependent wave vector,

$$\Delta X^{(J, K_{x0})} = D_1^{(J, K_{x0})} Z + X \quad (\text{A10})$$

is the distance from envelope center along the propagation direction and

$$W^{(J, K_{x0})}(Z) = W_x \sqrt{1 + \left(\frac{2D_2^{(J, K_{x0})} Z}{W_x^2} \right)^2} \quad (\text{A11})$$

reflects the evolution of the envelope width. The output amplitude is thus a linear superposition of modes from the different bands with a Gaussian envelope and wave vector slowly dependent on distance from beam center. Extra phase shifts due to diffraction are also added to the phase expected from single-mode propagation. Except for particular excitation wave vectors K_{x0} , located at Brillouin zone edges, the beams of the different FB modes do not overlap spatially because they are diffracted in different directions ($D_1^{(J, K_{x0})}$ varies with J). As a result, far enough from such wave vectors, the modes do not interfere and a single mode J contributes. Then, neglecting the wave vector dependence of the FB modes in the vicinity of K_{x0} , the guided output intensity profiles behind a one-dimensional waveguide array excited by a Gaussian beam can be written

$$I(J, K_{x0}, X, Y, Z) \approx |U(J, K_{x0}, X, Y)|^2 |\overline{U}_p^*(J, K_{x0})|^2 \times \frac{S^2}{\pi W_x W(J, K_{x0}, Z)} e^{-2\left(\frac{X + D_1^{(J, K_{x0})} Z}{W(J, K_{x0}, Z)}\right)^2}, \quad (\text{A12})$$

where the superscripts (J, K_{x0}) are lowered for clarity. In Eq. (A12), $|U(J, K_{x0}, X, Y)|^2$ and the Gaussian profile

This Fourier transform can be approximated developing K_z around $K_{x0} - pG$ to second order,

$$K_z(J, K_x) \approx K_z(J, K_{x0}) + D_1^{(J, K_{x0})}(K_x - K_{x0} + pG) + \frac{D_2^{(J, K_{x0})}}{2}(K_x - K_{x0} + pG)^2, \quad (\text{A7})$$

and F_p to first order since, in weakly and moderately coupled arrays and with the exception of shallow bands, the periodic part of the Bloch modes only slowly depends on the wave vector. Hence

reflect the underlying FB mode and its envelope, respectively. Finally, making use of the normalization condition $\sum_q |\overline{U}_q(J, K_{x0})|^2 = 1$, a field coupling efficiency into mode J at wave vector K_{x0} can be written as

$$T(J, K_{x0}) = |\overline{U}_p(J, K_{x0})|^2. \quad (\text{A13})$$

APPENDIX B

We detail here on the example of an interface between two semi-infinite arrays I and II of coupling constants C_1 and C_2 , the choices of the elements of matrices C and O . From Ref. [18] and using a hat to denote nonreduced coupling coefficients $\hat{\xi} = \xi C$ and $\hat{\zeta} = \zeta C$, the parameter $\hat{\xi}_1$ in a homogeneous array referred to as I is proportional to

$$2\langle 101 \rangle_I = \langle 0\bar{1}0 \rangle_I + \langle 010 \rangle_I. \quad (\text{B1})$$

At an interface between two arrays I and II having identical ridges but different separation distances between them, $\hat{\xi}$ is proportional to

$$\langle 0\bar{1}0 \rangle_I + \langle 010 \rangle_{II}, \quad (\text{B2})$$

so that

$$\hat{\xi} = \frac{\hat{\xi}_1 + \hat{\xi}_2}{2}. \quad (\text{B3})$$

The other $\hat{\xi}$ coefficients are equal to their value in the homogeneous arrays I or II.

Then, the ratio of second to first neighbor coupling coefficients in an array, I for instance, can be expressed as a function of coupling ratios as

$$\frac{\hat{\zeta}_1}{C_1} = \frac{\langle \bar{1}01 \rangle_I + \langle 002 \rangle_I}{\langle 001 \rangle_I} = \frac{\langle 002 \rangle_I}{\langle 001 \rangle_I} \left(1 + \frac{\langle \bar{1}01 \rangle_I}{\langle 002 \rangle_I} \right). \quad (\text{B4})$$

The coupling ratio before the parentheses is first order (second order over first order) in evanescent coupling, whereas

that within the parentheses is 0th order. If evanescent coupling between the individual waveguides can be characterized by a single evanescence distance L_e , the 0th-order coupling ratios do not depend on the ridge separation S , or $s = S/L_e$, while first-order ratios vary as e^{-s} . As a result,

$$\frac{\hat{\zeta}_2}{C_2} \frac{C_1}{\hat{\zeta}_1} = e^{-(s_2-s_1)}. \quad (\text{B5})$$

Then, for an interface waveguide, the second- to first-neighbor coupling coefficient ratio toward array II is

$$\frac{\hat{\zeta}}{C} = \frac{\langle 022 \rangle_{\text{II}}}{\langle 011 \rangle_{\text{II}}} \left(1 + \frac{\langle 012 \rangle_{\text{II}}}{\langle 022 \rangle_{\text{II}}} \right) = \frac{\hat{\zeta}_2}{C_2}, \quad (\text{B6})$$

where $C = C_2$, so that $\hat{\zeta} = \hat{\zeta}_2$. For a waveguide in array I immediately adjacent to the interface, the same ratio toward

array II is

$$\begin{aligned} \frac{\hat{\zeta}}{C} &= \frac{\langle \bar{1}11 \rangle_{\text{I-II}}}{\langle \bar{1}00 \rangle_{\text{I}}} \left(1 + \frac{\langle \bar{1}01 \rangle_{\text{I-II}}}{\langle \bar{1}11 \rangle_{\text{I-II}}} \right) \\ &= \frac{\langle \bar{1}11 \rangle_{\text{I-II}}}{\langle \bar{1}11 \rangle_{\text{I}}} \times \frac{\langle \bar{1}11 \rangle_{\text{I}}}{\langle \bar{1}00 \rangle_{\text{I}}} \left(1 + \frac{\langle \bar{1}01 \rangle_{\text{I}}}{\langle \bar{1}11 \rangle_{\text{I}}} \right) \\ &= e^{-(s_2-s_1)} \frac{\hat{\zeta}_1}{C_1} = \frac{\hat{\zeta}_2}{C_2}, \end{aligned} \quad (\text{B7})$$

where $C = C_1$, so that

$$\hat{\zeta} = \hat{\zeta}_2 \frac{C_1}{C_2}. \quad (\text{B8})$$

Such rules have to be combined when a waveguide belongs to several categories, e.g., when it is an interface and also adjacent to another interface, or adjacent to two distinct interfaces.

-
- [1] D. N. Christodoulides, F. Lederer, and Y. Silberberg, *Nature* **424**, 817 (2003).
- [2] J. W. Fleischer, G. Bartal, O. Cohen, T. Schwartz, O. Manela, B. Freedman, M. Segev, H. Buljanm, and N. K. Efremidis, *Opt. Express* **13**, 1780 (2005).
- [3] H. S. Eisenberg, Y. Silberberg, R. Morandotti, and J. S. Aitchison, *Phys. Rev. Lett.* **85**, 1863 (2000).
- [4] T. Pertsch, P. Dannberg, W. Elflein, A. Bräuer, and F. Lederer, *Phys. Rev. Lett.* **83**, 4752 (1999).
- [5] R. Morandotti, U. Peschel, J. S. Aitchison, H. S. Eisenberg, and Y. Silberberg, *Phys. Rev. Lett.* **83**, 4756 (1999).
- [6] F. Dreisow, A. Szameit, M. Heinrich, T. Pertsch, S. Nolte, A. Tünnermann, and S. Longhi, *Phys. Rev. Lett.* **101**, 143602 (2008).
- [7] T. Schwartz, G. Bartal, S. Fishman, and M. Segev, *Nature* **446**, 52 (2007).
- [8] Y. Lahini, A. Avidan, F. Pozzi, M. Sorel, R. Morandotti, D. N. Christodoulides, and Y. Silberberg, *Phys. Rev. Lett.* **100**, 013906 (2008).
- [9] K. G. Makris, D. N. Christodoulides, O. Peleg, M. Segev, and D. Kip, *Opt. Express* **16**, 10309 (2008).
- [10] D. N. Christodoulides and E. D. Eugenieva, *Phys. Rev. Lett.* **87**, 233901 (2001).
- [11] A. Fratallocchi, G. Assanto, K. A. Brzdakiewicz, and M. A. Karpierz, *Appl. Phys. Lett.* **86**, 051112 (2005).
- [12] R. A. Vicencio, M. I. Molina, and Y. S. Kivshar, *Phys. Rev. E* **70**, 026602 (2004).
- [13] H. Trompeter, U. Peschel, T. Pertsch, F. Lederer, U. Strepel, D. Michaelis, and A. Bräuer, *Opt. Express* **11**, 3404 (2003).
- [14] J. M. Moison, N. Belabas, Ch. Minot, and J. A. Levenson, *Opt. Lett.* **34**, 2462 (2009).
- [15] R. A. Syms, *IEEE J. Quantum Electron.* **23**, 525 (1987).
- [16] A. Szameit, H. Trompeter, M. Heinrich, F. Dreisow, U. Peschel, T. Pertsch, S. Nolte, F. Lederer, and A. Tünnermann, *New J. Phys.* **10**, 103020 (2008).
- [17] N. Belabas, S. Bouchoule, I. Sagnes, J. A. Levenson, Ch. Minot, and J. M. Moison, *Opt. Express* **17**, 3148 (2009).
- [18] Ch. Minot, N. Belabas, J. A. Levenson, and J. M. Moison, *Opt. Express* **18**, 7157 (2010).
- [19] H. S. Eisenberg, Y. Silberberg, R. Morandotti, A. R. Boyd, and J. S. Aitchison, *Phys. Rev. Lett.* **81**, 3383 (1998).
- [20] C. E. Rüter, J. Wisniewski, and D. Kip, *Opt. Lett.* **31**, 2768 (2006).
- [21] T. Pertsch, T. Zentgraf, U. Peschel, A. Bräuer, and F. Lederer, *Phys. Rev. Lett.* **88**, 093901 (2002).
- [22] R. Zengerle, *J. Mod. Opt.* **34**, 1589 (1987).
- [23] D. Mandelik, H. S. Eisenberg, Y. Silberberg, R. Morandotti, and J. S. Aitchison, *Phys. Rev. Lett.* **90**, 053902 (2003).
- [24] D. Mandelik, R. Morandotti, J. S. Aitchison, and Y. Silberberg, *Phys. Rev. Lett.* **92**, 093904 (2004).
- [25] Y. Lahini, D. Mandelik, and Y. Silberberg, *Opt. Express* **13**, 1762 (2005).
- [26] C. E. Rüter and D. Kip, *Phys. Rev. A* **77**, 013818 (2008).
- [27] R. Dong, C. E. Rüter, D. Kip, J. Cuevas, P. G. Kevrekidis, D. Song, and J. Xu, *Phys. Rev. A* **83**, 063816 (2011); R. Dong, C. E. Rüter, D. Song, J. Xu, and D. Kip, *Opt. Express* **18**, 27493 (2010).
- [28] A. A. Sukhorukov, D. Neshev, W. Krolikowski, and Y. S. Kivshar, *Phys. Rev. Lett.* **92**, 093901 (2004).
- [29] J. Meier, G. I. Stegeman, D. N. Christodoulides, Y. Silberberg, R. Morandotti, H. Yang, G. Salamo, M. Sorel, and J. S. Aitchison, *Phys. Rev. Lett.* **92**, 163902 (2004).
- [30] S. Suntsov, K. G. Makris, D. N. Christodoulides, G. I. Stegeman, R. Morandotti, M. Volatier, V. Aimez, R. Arès, C. E. Rüter, and D. Kip, *Opt. Express* **15**, 4663 (2007).
- [31] R. Iwanow, R. Schiek, G. Stegeman, T. Pertsch, F. Lederer, Y. Min, and W. Sohler, *Opto-Electronics Rev.* **13**, 113 (2005).
- [32] Y. Linzon, Y. Sivan, B. Malomed, M. Zaezjev, R. Morandotti, and S. Bar-Ad, *Phys. Rev. Lett.* **97**, 193901 (2006).
- [33] P. Yeh, A. Yariv, and C. S. Hong, *J. Opt. Soc. Am.* **67**, 423 (1977).

- [34] F. Chen, M. Stepić, C. E. Rüter, D. Runde, D. Kip, V. Shandarov, O. Manela, and M. Segev, *Opt. Express* **13**, 4314 (2005).
- [35] A. A. Sukhorukov, D. N. Neshev, and Y. S. Kivshar, *Opt. Express* **15**, 13058 (2007).
- [36] E. Kapon, J. Katz, and A. Yariv, *Opt. Lett.* **9**, 125 (1984).
- [37] N. Belabas, Ch. Minot, J. A. Levenson, and J. M. Moison, *J. Lightwave Technol.* **29**, 3009 (2011).
- [38] F. Lederer, G. I. Stegeman, D. N. Christodoulides, G. Assanto, M. Segev, and Y. Silberberg, *Phys. Rep.* **463**, 1 (2008), and references therein.